Journal of
Applied Remote Sensing

RemoteSensing.SPIEDigitalLibrary.org

Locating and monitoring of landslides based on small baseline subset interferometric synthetic aperture radar

Guijie Wang
Yunlong Wang
Xisheng Zang
Juyan Zhu
Weilun Wu

SPIE.

Guijie Wang, Yunlong Wang, Xisheng Zang, Juyan Zhu, Weilun Wu, "Locating and monitoring of landslides based on small baseline subset interferometric synthetic aperture radar," *J. Appl. Remote Sens.* **13**(4), 044528 (2019), doi: 10.1117/1.JRS.13.044528.

Locating and monitoring of landslides based on small baseline subset interferometric synthetic aperture radar

Guijie Wang,[a,*] Yunlong Wang,[a] Xisheng Zang,[a] Juyan Zhu,[a] and Weilun Wu[b]

[a]China Institute of Geo-Environment Monitoring, Beijing, China
[b]Beijing Jingyan Geotechnical Consultants Ltd., Beijing, China

Abstract. Due to the effects of rugged terrain and vegetation cover, improving the locating and monitoring accuracy of time series interferometric synthetic aperture radar (TS-InSAR) in detecting the development of landslides in mountainous and valley areas has become a problem that needs to be solved. Our study uses the ground local incident angle (GLIA) to locate noneffective monitoring areas that are affected by steep terrain as well as to improve the locating accuracy of TS-InSAR technology in the effective coverage area. At the same time, the improved small baseline subset InSAR (SBAS-InSAR) method is used to improve the density of interferometer targets as well as to solve the problem of insufficient permanent scatterers due to the effects of vegetation coverage. A geometric model of GLIA was established. Ascending and descending synthetic aperture radar (SAR) data from the Advanced Land Observation Satellite (ALOS) were used for calculating the value of GLIA. The relationships of the GLIA and the interference characteristics of InSAR data were analyzed, and the locations of noneffective areas were determined. Finally, 19 ascending pass SAR data scenes acquired by the ALOS-1 satellite were processed through using the improved SBAS-InSAR method, and the detailed time series moving displacement information from 2007 to 2011 was mapped in Wudongde hydropower reservoir. Furthermore, the potentially moving landslide areas and landslide hazard areas were located in the effective interference areas. The active Jinpingzi landslide was investigated in detail, and the single-point monitoring results of SBAS-InSAR were compared with the electronic total station (ETS) measurement results. The conclusion shows that the monitoring results of SBAS-InSAR were in agreement with the ground field survey and the single-point ETS monitoring, and the applicability of the model and algorithm proposed was proved. Our study provides a reference for the early identification and high-precision monitoring of landslides in mountainous and valley areas. [DOI: 10.1117/1.JRS.13.044528]

Keywords: landslide; locating; monitoring; ground local incidence angle; small baseline subset interferometric synthetic aperture radar; effective interference region.

Paper 190716 received Sep. 12, 2019; accepted for publication Dec. 2, 2019; published online Dec. 24, 2019.

1 Introduction

Interferometric synthetic aperture radar (InSAR) has come to provide an important type of technology for monitoring wide-area and long-term ground movement. It has been widely applied to survey areas with landslides. Achache et al.[1] demonstrated the ability of InSAR to monitor small displacements at the scale required for large landslide monitoring and acquired the same trend as that of ground-based measurements. Soon after, Fruneau et al.,[2] Vietmeier et al.,[3] Rizzo and Tesauro,[4] and Squarzoni et al.[5] began to apply InSAR technology in landslide monitoring and compared the trends and results with ground-based measurements. Then, international experts and scholars carried out more in-depth studies of the application of the InSAR technique to landslide monitoring, and the emphasis of research changed from validation of monitoring

*Address all correspondence to Guijie Wang, E-mail: wanggj@cigem.cn

results to quantitative analysis of monitoring accuracy.[6–12] Next, high-accuracy monitoring methods, including persistent scatterer InSAR,[13] small baseline subset InSAR (SBAS-InSAR),[14] coherent point target,[15] stable point network,[16] StaMPS,[17] and SqueeSAR,[18] were proposed and applied.[19–35] To further improve region investigation and monitoring accuracy of landslides, InSAR has been combined with optical remote sensing, Global Navigation Satellite System, corner reflectors, and ground-based radar.[36–45] However, due to the influence of complex regional topography and land use, improving the locating and monitoring accuracy of time series (TS)-InSAR in detecting the development of regional landslides remains a problem that urgently needs to be solved. Plank et al.[46] presented a geographical information system procedure to predict the areas of layover and shadowing due to the geometric distortion of radar image caused by rugged terrain. Notti et al.[47] used various persistent scatterer interferometry techniques to map and monitor landslides in various mountainous environments to improve the extraction density of permanent scatterer. Wang et al.[48] and Xie et al.[49] also carried out studies on the location and monitoring of landslides in alpine canyon areas by applying InSAR technology.

This work aimed to overcome the influence of regional rugged terrain and vegetation cover as well as to improve the landslide monitoring accuracy of TS-InSAR in the Wudongde hydropower reservoir, which is a typical disaster-prone area of the mountain valley in western China. Based on former experiences, the ground local incident angle (GLIA), which represents the comprehensive factors of complex topography and satellite attitude parameters, was put forward, and the improved SBAS-InSAR method was used. A geometric model of GLIA was established. Each ground point value of GLIA was calculated and reclassified for the ascending and descending synthetic aperture radar (SAR) data from the Advanced Land Observation Satellite (ALOS) in the study area so that the noneffective interference areas could be determined. Finally, 19 ascending SAR data scenes acquired by the ALOS-1 satellite were processed using the improved SBAS-InSAR method, and the detailed time series moving displacement information from 2007 to 2011 was mapped in the effective interference region. The potentially moving landslide areas and landslide hazard areas were located, and the active Jinpingzi landslide was investigated in detail. The single-point monitoring results of SBAS-InSAR were compared with the electronic total station (ETS) measurement results. The monitoring results of the SBAS-InSAR were in perfect agreement with the ground manual survey and the single-point ETS monitoring. Therefore, the locating and monitoring accuracy of TS-InSAR in detecting the development of landslides in mountainous and valley areas were improved, and the applicability of the model and algorithm proposed was proved.

2 Materials and Methods

2.1 *Study Site*

The study area lies in the vicinity of Wudongde hydropower reservoir at the junction of Luquan and Huidong counties in Yunnan and Sichuan provinces, China, respectively, as shown in Fig. 1, and the study area is about 400 km^2. The hydropower station is located in the downstream reach of Jinsha River, which cuts to a depth of about 1000 to 2000 m in the Wudongde hydropower reservoir region. Elevations range from 2000 to 3500 m above sea level on both sides of the valley, which has an average slope of >30 deg to 45 deg. The exposed Cenozoic, Mesozoic, Paleozoic, and Mesoproterozoic strata in the reservoir area mainly include Quaternary, Cretaceous–Jurassic, Triassic, Permian, Cambrian, Sinian, Gabbro, and Granite, as shown in Fig. 2. Therefore, the rising and falling water level in the reservoir can lead to adverse changes in the geologic and anthropomorphic environment that have resulted in the occurrence of landslides at all scales on the surrounding slopes. In particular, the Jinpingzi landslide, which occurred about 900 m from the dam site, directly affects the safety and normal operation of the reservoir. A background map of the study field is shown in Fig. 1, and the suspected landslides are the areas whose features were found to be very similar to the landslide in the field survey. The investigated area is framed in a purple square in this figure and represented by a red circle in the vicinity map; detailed information (zonation and ETS point arrangement) of the Jinpingzi landslide is inserted in the lower right corner.

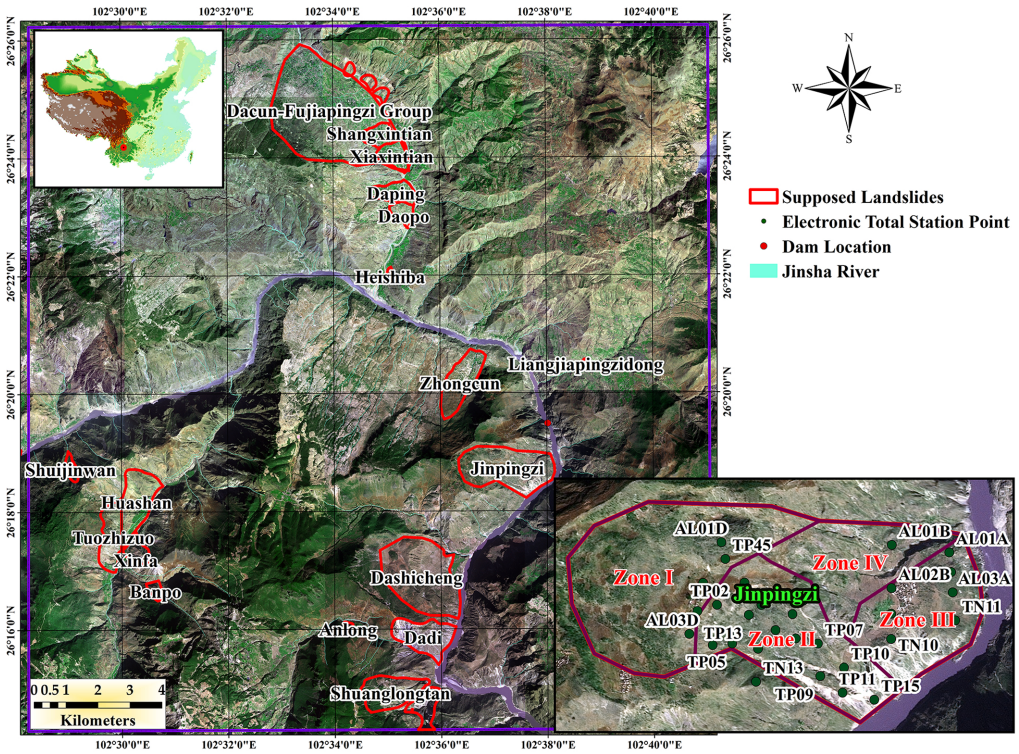

Fig. 1 Topographically shaded aerial photo showing names and outlines of supposed landslide areas in the study area. A vicinity map in the upper left shows the location of the study area within China. An inset map in the lower right shows the zones and ETS monitoring sites within the Jinpingzi landslide area.

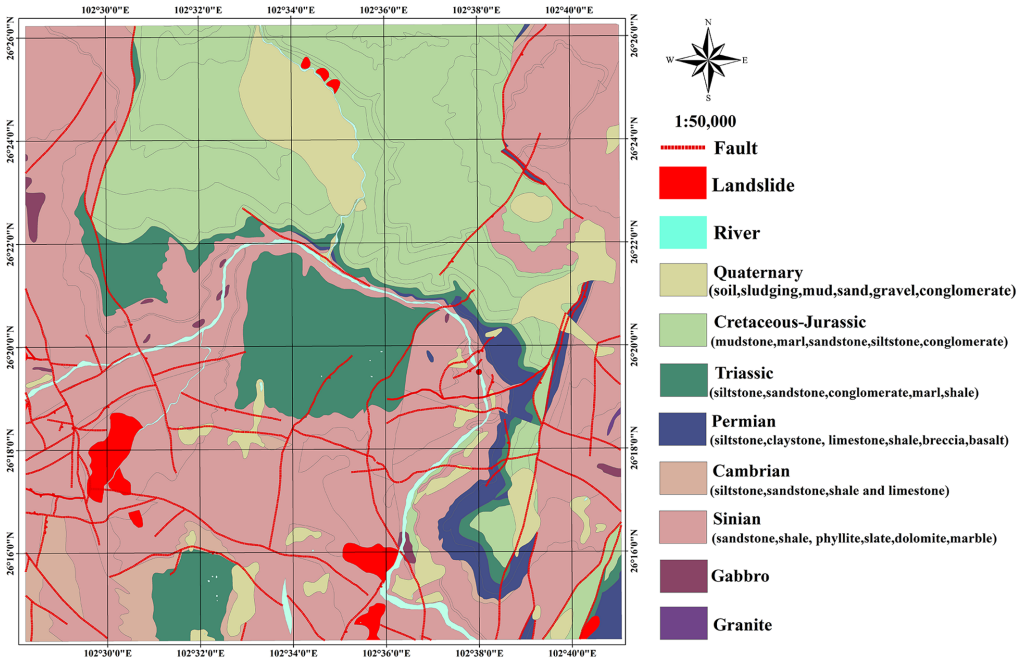

Fig. 2 Geologic map of the study region.

2.2 *Available Data*

Nineteen scenes of phased array-type L-band synthetic aperture radar (PALSAR-1) ascending acquisitions of the ALOS-1 satellite and two scenes of PALSAR-2 descending acquisitions of ALOS-2, with a wavelength of 230 mm (L-band), were applied. The Shuttle Radar Topography Mission digital elevation models (DEMs) (3 arc sec) were interpolated and corrected to provide auxiliary 10-m DEM data. The parameters of PALSAR data are shown in Table 1.The spatial baseline of the two scenes of PALSAR-2 descending acquisitions was 97 m. The time-position plot of the 19 PALSAR-1 ascending acquisitions is shown in Fig. 3. The minimum and the

Table 1 Parameters of the available PALSAR data.

Serial number	Observation date	Polarization mode	Center latitude (deg)	Center longitude (deg)	Center incident angle (deg)	Center azimuth angle (deg)	Temporal baseline (day)	Orbital model	Satellite
0	July 12, 2007	FBD/HH	26.254	102.409	38.747	84.060	0	Ascending	ALOS-1
1	August 27, 2007	FBD/HH	26.251	102.408	38.724	84.084	46	Ascending	
2	October 12, 2007	FBD/HH	26.250	102.414	38.734	84.097	92	Ascending	
3	January 12, 2008	FBS/HH	26.248	102.417	38.732	84.114	184	Ascending	
4	February 27, 2008	FBS/HH	26.250	102.421	38.732	84.104	230	Ascending	
5	April 13, 2008	FBS/HH	26.253	102.426	38.740	84.088	276	Ascending	
6	July 14, 2008	FBD/HH	26.253	102.397	38.729	84.064	368	Ascending	
7	August 29, 2008	FBD/HH	26.252	102.373	38.714	84.052	414	Ascending	
8	October 14, 2008	FBD/HH	26.252	102.389	38.747	84.060	460	Ascending	
9	November 29, 2008	FBS/HH	26.250	102.393	38.756	84.077	506	Ascending	
10	March 1, 2009	FBS/HH	26.251	102.395	38.741	84.077	598	Ascending	
11	September 1, 2009	FBD/HH	26.252	102.404	38.735	84.066	782	Ascending	
12	October 17, 2009	FBD/HH	26.249	102.407	38.735	84.094	828	Ascending	
13	January 17, 2010	FBS/HH	26.250	102.411	38.746	84.096	920	Ascending	
14	July 20, 2010	FBD/HH	26.253	102.416	38.733	84.074	1104	Ascending	
15	September 4, 2010	FBD/HH	26.252	102.417	38.723	84.090	1150	Ascending	
16	December 5, 2010	FBD/HH	26.249	102.422	38.744	84.117	1242	Ascending	
17	January 20, 2011	FBS/HH	26.251	102.423	38.739	84.105	1288	Ascending	
18	March 7, 2011	FBS/HH	26.248	102.433	38.757	84.131	1334	Ascending	
19	January 3, 2015	FBS/HH	26.283	102.425	42.901	−82.398	0	Descending	ALOS-2
20	January 2, 2016	FBS/HH	26.823	102.425	42.903	−82.398	364	Descending	

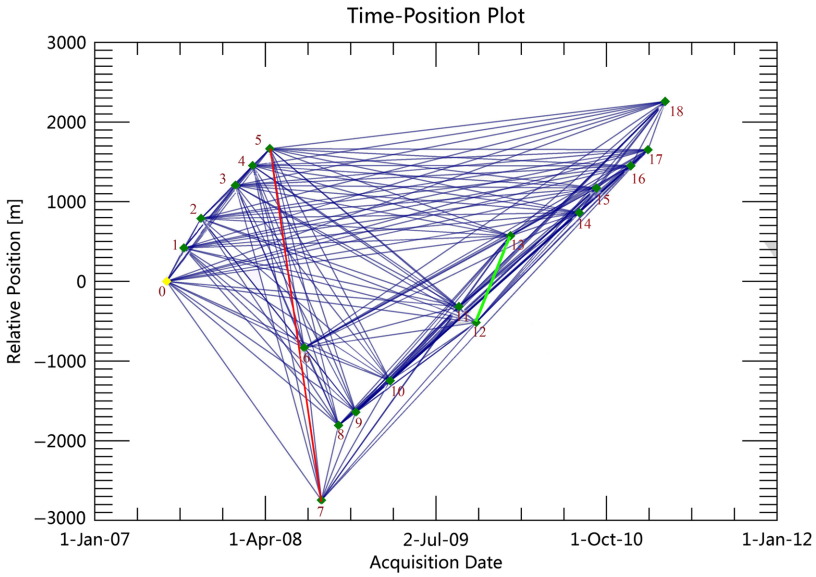

Fig. 3 Time-position plot of the 19 ascending pass data scenes (the yellow point is the master image).

maximum spatial baselines were 205 and 4392 m, which are represented by green and red lines in Fig. 3, respectively.

2.3 *Small Baseline Subset Interferometric Synthetic Aperture Radar Technology*

The conventional SBAS-InSAR[14] is a time series-based technique and is considered advanced compared to conventional InSAR. The proposed SBAS-InSAR is an improvement on the conventional SBAS-InSAR method. The proposed SBAS-InSAR introduced phase coherence of lower threshold into the inverse model, instead of discarding any noisy data present in a fraction of the interferograms. All the pixels were retained in the processing chain, and the weight of the observed phase data was based on the coherence of each pixel in each differential interferogram using a weighting matrix. The specific data processes are shown in Fig. 4.

2.4 *Ground Local Incidence Angle and its Calculation Model*

The GLIA is defined as the intersection angle between the propagation vector of the radar wave and the surface normal of a ground point. It is determined by the incidence and azimuth angles of the satellite as well as the slope and aspect of each ground point.[47–49]

A geometric sketch of GLIA is shown in Fig. 5, where θ is the incident angle, which is the angle between the radar wave propagation vector and the vertical direction, ∂ is the local slope angle of the ground point, and θ_{loc} is the GLIA. The δ and ω are the local aspect angle of the ground point and the horizontal angles of line of sight (LOS) direction, respectively, where they are clockwise rotational horizontal angles and their zero direction is the north. Finally, $\mathbf{V_s}$, $\mathbf{V_n}$, and $\mathbf{V_a}$ are the vector of LOS direction, the vector of the ground point normal direction, and the vector composition of $\mathbf{V_s}$ and $\mathbf{V_n}$, respectively.

Thus, under the right sight condition, ω can be expressed as $\omega =$ azimuth angle $+90$ deg; under the left sight condition, $\omega =$ azimuth angle -90 deg. The right sight condition is shown in Fig. 5, as an example. The three components of $\mathbf{V_s}$ can be written using Eqs. (1)–(3):

$$X_{V_s} = |\mathbf{V_s}| \times \sin\theta \times \cos\omega, \tag{1}$$

$$Y_{V_s} = |\mathbf{V_s}| \times \sin\theta \times \sin\omega, \tag{2}$$

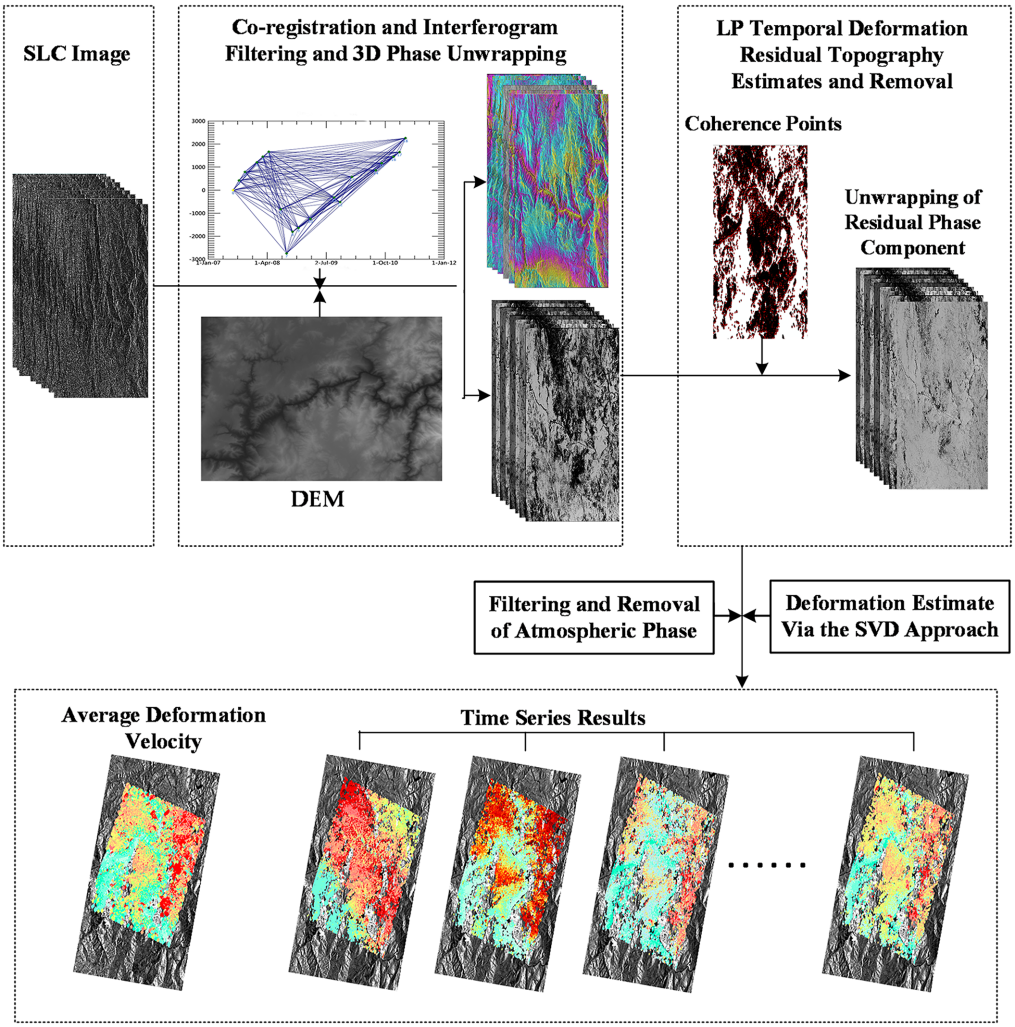

Fig. 4 Flowchart of SBAS-InSAR technology. Note: SLC, single-look complex; DEM, digital elevation model; LP, low pass; SVD, singular value decomposition.

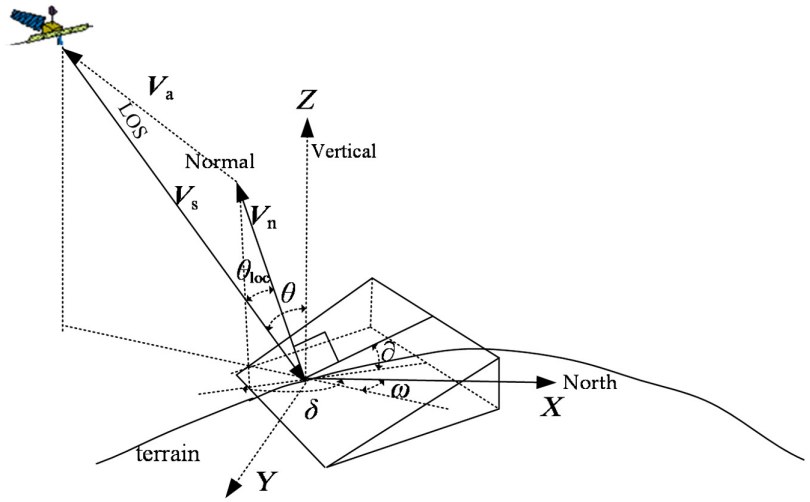

Fig. 5 Geometric sketch of the GLIA, where the three dimensions are shown as X, Y, and Z. Note: θ, incidence angle; θ_{loc}, GLIA; δ, local aspect angle of the ground point; ∂, local slope angle of the ground point; ω, horizontal angles of LOS direction.

$$Z_{V_s} = -|\mathbf{V_s}| \times \cos\,\theta. \tag{3}$$

The three components of $\mathbf{V_n}$ can be written using Eqs. (4)–(6):

$$X_{V_n} = |\mathbf{V_n}| \times \sin\partial \times \cos\delta, \tag{4}$$

$$Y_{V_n} = |\mathbf{V_n}| \times \sin\partial \times \sin\delta, \tag{5}$$

$$Z_{V_n} = |\mathbf{V_n}| \times \cos\partial. \tag{6}$$

Thus, the three components of $\mathbf{V_a}$ can be written using Eqs. (7)–(9):

$$X_{V_a} = X_{V_n} + X_{V_s}, \tag{7}$$

$$Y_{V_a} = Y_{V_n} + Y_{V_s}, \tag{8}$$

$$Z_{V_a} = Z_{V_n} + Z_{V_s}. \tag{9}$$

Based on cosine law:

$$|\mathbf{V_a}|^2 = |\mathbf{V_n}|^2 + |\mathbf{V_s}|^2 + 2|\mathbf{V_n}| \times |\mathbf{V_s}| \times \cos\,\theta_{\text{loc}}. \tag{10}$$

Thus,

$$\theta_{\text{loc}} = \text{arc}\,\cos[\cos\partial \times \cos\,\theta - \sin\,\theta \times \sin\partial \times \cos(\omega - \delta)]. \tag{11}$$

2.5 *Analysis of the Reliable Interference Region*

2.5.1 *Calculation of GLIA*

Both ascending and descending data from ALOS PALSAR were used in this study. The θ and ω data for every ground point could be calculated using the ALOS PALSAR data; ∂ and δ were obtained from the DEM (10-m spatial resolution) raster data spatial analysis.

According to Eq. (11), the GLIA of every point can be obtained. The range of GLIA values for the ascending and descending data were 26.58 deg to 101.97 deg and 32.51 deg to 116.50 deg, respectively. Negative values of GLIA represent layover areas (an overlapping of radar responses from different positions), whereas the values of GLIA higher than 90 deg represent shadowed areas (e.g., areas behind steep mountains, which are not illuminated by the radar beam). The values of GLIA at each point show differences over area. For the sake of simplicity in the following analysis, the values of GLIA were reclassified into groups with the interval of 10 deg (considering DEM data of 10-m resolution and radar data of ALOS-1 are used); values of GLIA representing layover and shadowed areas were placed into two other groups, separately. Therefore, the 11 angle groups were scattered in the study area as shown in Figs. 6 and 7.

2.5.2 *Correlation analysis of the GLIA and interference characteristics*

The interference characteristics form a description of the interference capability indices of the InSAR data set. This study mainly refers to the backscattering coefficient (BSC) and coherence coefficient (CC) of the InSAR data set. The BSC is the ratio of the grayscale value of each pixel to the maximum grayscale value (255) in power images.

To acquire the relationship of GLIA and backward scattering elements, the average values of BSCs were computed for the ascending and descending SAR images. The average values of BSC as a regional statistic were obtained according to the reclassified interval of GLIA. The specific variation trends of GLIA and BSC are shown in Fig. 8, in which BSC is the average value of all pixels in the mean power image rather than the average value of all interference point targets for the SBAS-InSAR.

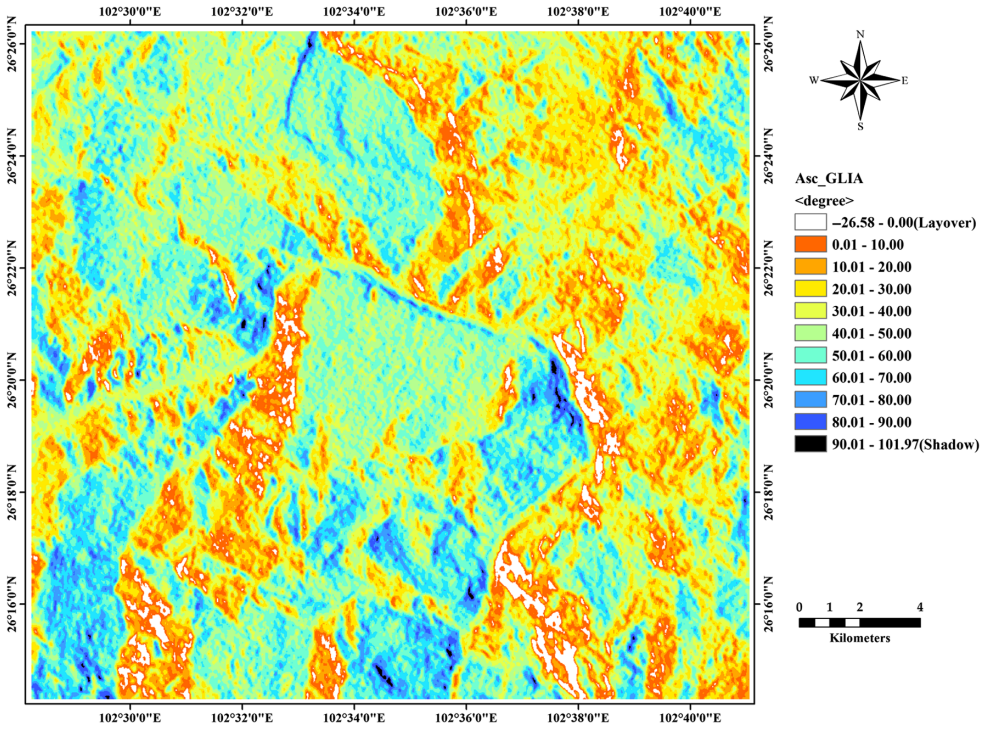

Fig. 6 Distribution and reclassification map of the GLIA for the ascending pass data.

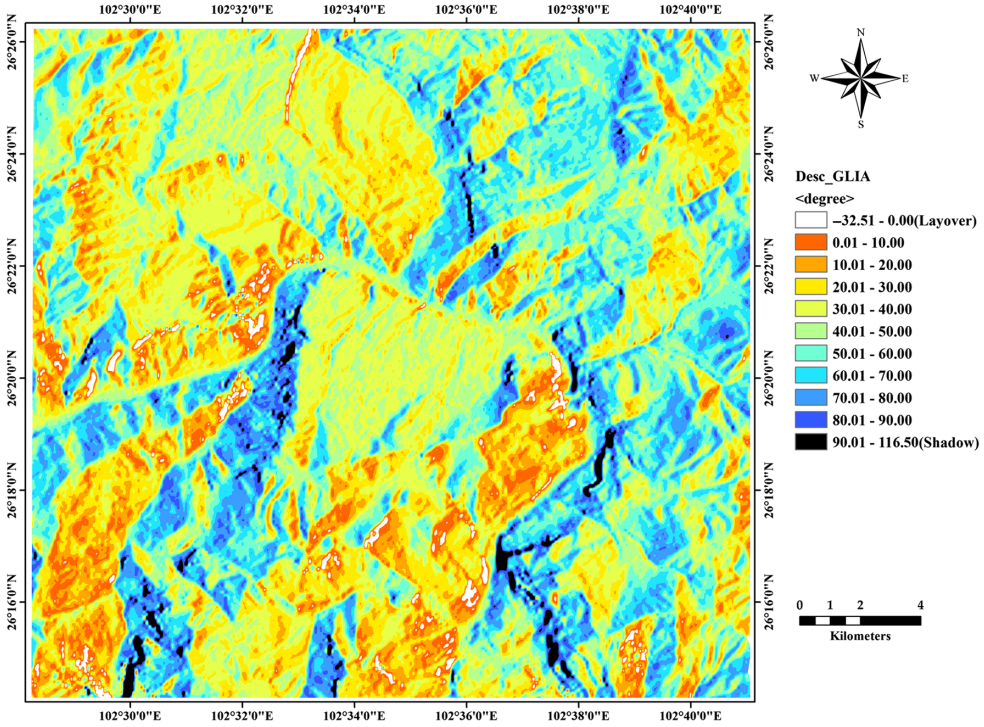

Fig. 7 Distribution and reclassification map of the GLIA for the descending pass data.

The BSC decreased with an increase in GLIA (Fig. 8). However, the values of BSC were higher and more stable in ascending data with less than a 10-deg interval and in descending data with less than a 30-deg interval. Then, the gradient variation exhibited rapid slowing down after the 50-deg to 60-deg interval for both of the ascending and descending data. The BSC values were almost highest in the layover areas, but they were lowest in the shadowed areas.

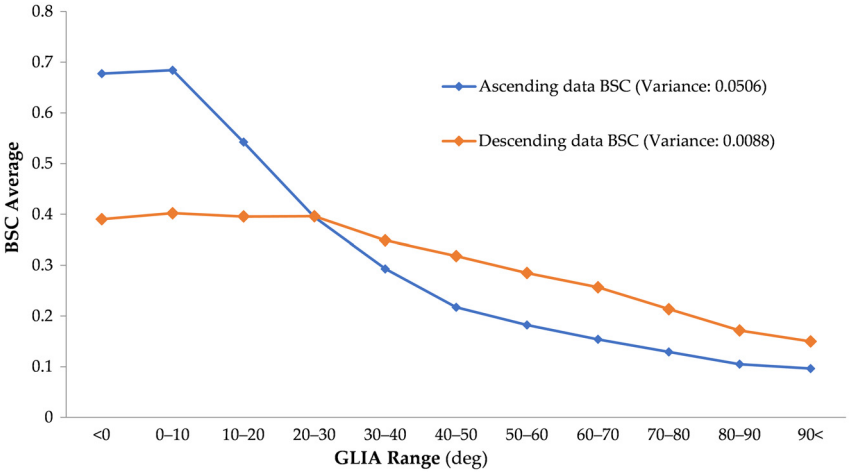

Fig. 8 Variation trend diagram of the BSC and the GLIA.

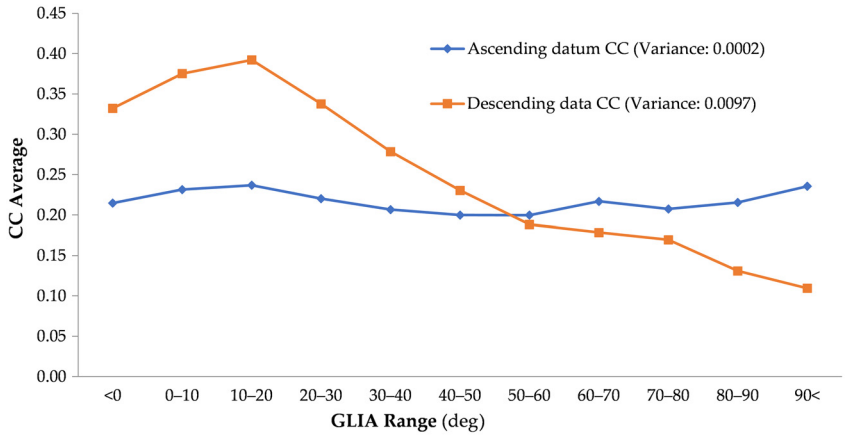

Fig. 9 Variation trend diagram of the CC and the GLIA.

To investigate the relationship between GLIA and coherence, the average values of the CC were computed according to the reclassified GLIA for the ascending and descending SAR images. The specific variation trends are shown in Fig. 9, in which CC is the average value of all pixels in the mean coherence image rather than the average value of all interference point targets for the SBAS-InSAR.

The average values of CC increased with an increase of the GLIA at first and peaked at 10 deg to 20 deg (Fig. 9). Then, the CC values declined with an increase of the GLIA. However, the CC value of the ascending data had a slight increasing trend after 50 deg to 60 deg, whereas the descending data continued to decline. This showed that the variation tendency was consistent and stable before 50 deg to 60 deg and that it had a different variation tendency after the 50-deg to 60-deg interval.

2.5.3 *Locating of the reliable interference region*

Several conclusions can be drawn based on Figs. 6 and 7 and the correlation of GLIA with both BSC (Fig. 8) and CC (Fig. 9). One can conclude that a smaller GLIA will produce a more intense backscatter in mountainous and valley areas. In addition, a smaller GLIA will also produce better interferometric properties in general for InSAR when applied in mountainous and valley areas. However, the detailed interference properties of SAR data were influenced by the ground target properties. Nevertheless, the interferometric properties of SAR data are relatively reliable with a

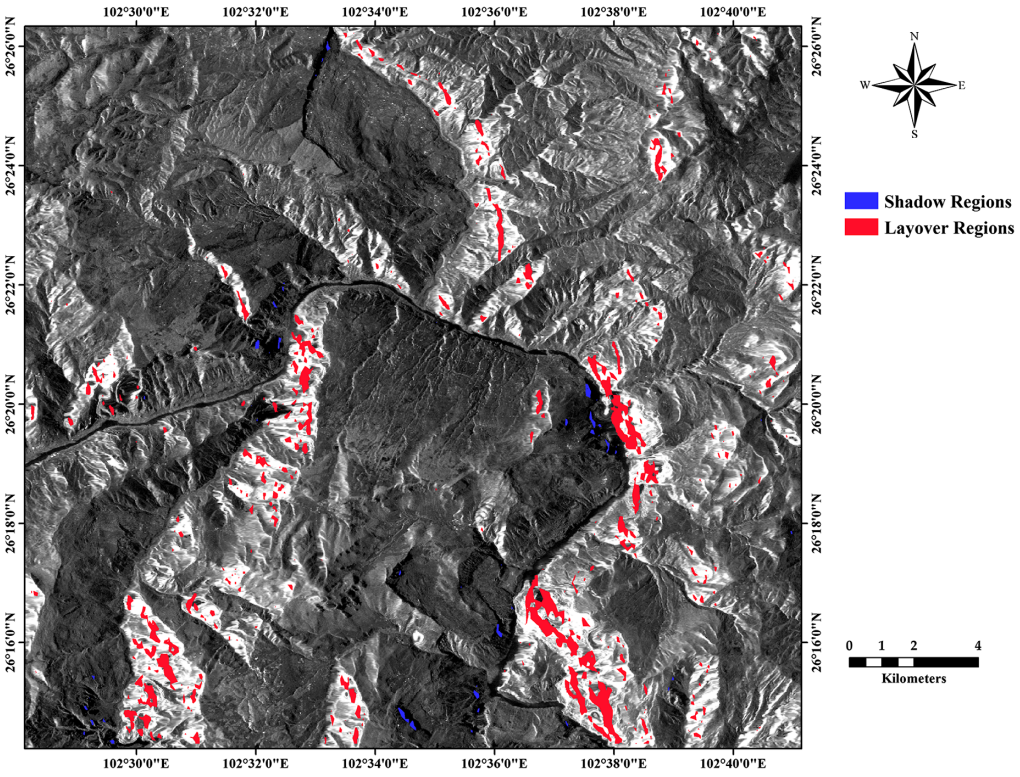

Fig. 10 Distribution map of effective interferometric regions.

1-deg to 90-deg range of GLIA. The layover (<0 deg) and shadowed (>90 deg) areas are noneffective for InSAR when applied in mountainous and valley areas.

In this work, the distribution of effective interferometric regions for the 19 PALSAR-1 ascending acquisition scenes is shown in Fig. 10. The red layover regions and the blue shadowed regions are both noneffective regions. The other gray regions for the 1-deg to 90-deg range of the GLIA are reliable interferometric regions.

3 Results

3.1 *Locating Results of Regional Landslides*

The displacement map (Fig. 11), which contains a detailed map showing the LOS moving average velocity, was obtained between July 12, 2007, and March 7, 2011, using the 19 PALSAR-1 ascending SAR image scenes with the SBAS-InSAR technique, and the gray areas are the noneffective interference areas marked "noneffective areas" in Fig. 11. The noneffective interference areas are not the absence of landslide disasters. They indicate that landslide disasters cannot be monitored using the 19 PALSAR-1 ascending SAR image scenes with the SBAS-InSAR technique in the noneffective interference areas. Other data or methods are needed for monitoring. Therefore, only the monitoring results of effective interference areas are analyzed in this study.

The annual deformation rate of the LOS was also obtained in Fig. 12. Red and brown polygons are used in Fig. 11 to mark landslides and debris flows, respectively, which have occurred or are in motion based on field survey.

In Figs. 11 and 12, the minus signs indicate areas of subsidence and the greater than zero indicate areas of uplift. The area of subsidence was investigated because landslide movement is always accompanied by subsidence. The velocity of the various points could be clearly identified, and the range of moving velocity was 0 to 89.44 mm/year (Fig. 11). The annual deformation rate of the LOS was slightly different (Fig. 12), but the variation trend was basically the same in different regions.

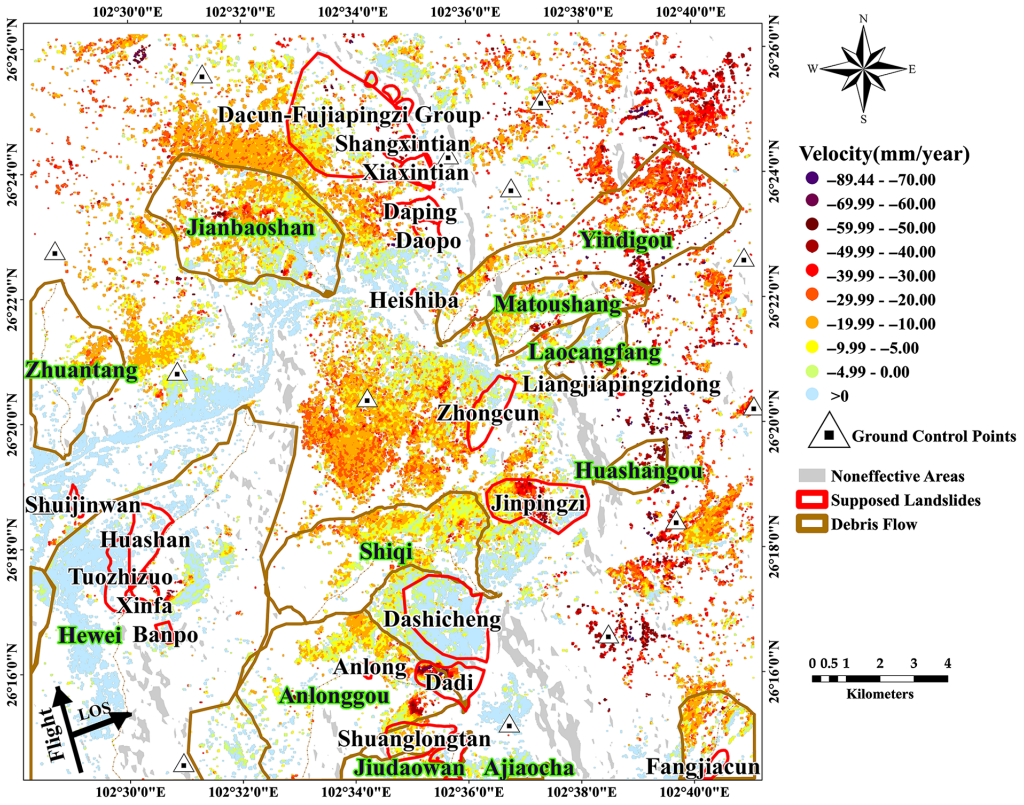

Fig. 11 Velocity map of LOS between July 12, 2007, and March 7, 2011, period.

Theoretically, the maximum detection capability of SAR system along the LOS is half of the wavelength by two SAR acquisitions,[10,50] and the wavelength of the L-band employed by PALSAR data was 230 mm. Therefore, considering the continuous change zone in the annual deformation rate in Fig. 12 and that the time period of the velocity was about 3.6 years in Fig. 11, the moving areas with velocity larger than 30 mm/year along the LOS direction were considered to be potentially moving landslide areas and landslide hazard areas.

As previously mentioned, the areas of brilliant color in Fig. 11, where the average velocity was larger than 30 mm/year, were mainly concentrated in the Jinpingzi landslide, at the mouth of the Anlonggou debris flow, in the catchments of the Yindigou and Matoushang debris flows, and in the Dacun-Fujiapingzi landslide group.

3.2 *Monitoring Results of the Jinpingzi Landslide*

To verify the accuracy of the improved SBAS-InSAR technique for the location and monitoring of the monomerous Jinpingzi landslide, the deformation evolution of this active landslide was investigated. The displacement maps of the LOS direction were obtained from July 12, 2007, to March 7, 2011 (Fig. 13). At the same time, the annual deformation rate in the LOS direction was also obtained (Fig. 14). The displacement value of every monitoring point was revealed, and the moving displacement of the different regions can be clearly identified in the displacement map. The Jinpingzi landslide can be divided into four zones, namely I, II, III, and IV (Fig. 13), based on the local stratigraphic composition of the slide material. The results (Figs. 14 and 15) show that the displacement of zone II and a partial region of zone I were the largest; these must be regarded as the most important potential landslide disaster areas needing further investigation. The displacement of the other zones was relatively small. However, note that zone III is experiencing relative uplift that may be caused by the effects of human activities that are already in progress. Therefore, the results obtained via SBAS-InSAR were consistent with those obtained via ground monitoring results, as shown in Fig. 13 and Table 2.

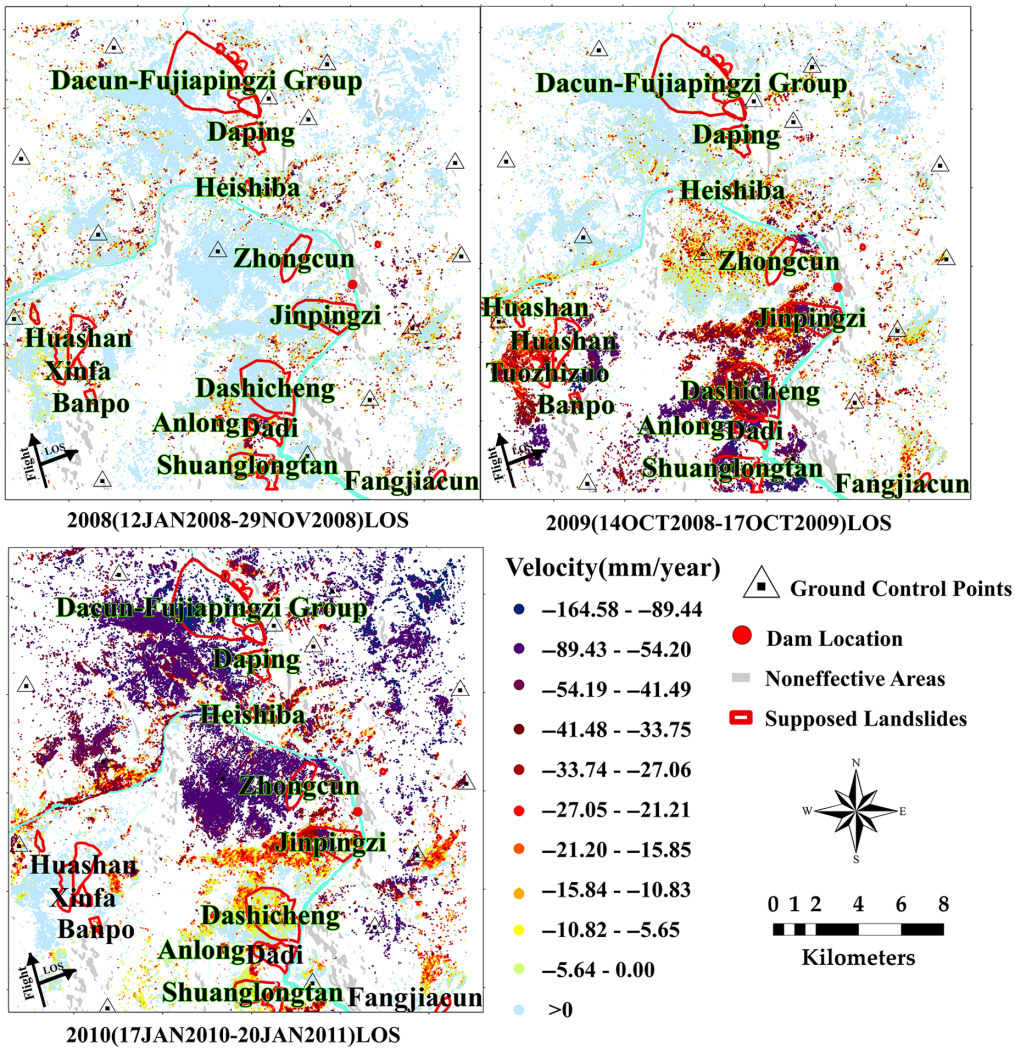

Fig. 12 Annual deformation rate of the LOS.

4 Discussion

4.1 *Locating Accuracy of Regional Landslides*

The SBAS-InSAR monitoring results compared with the field survey results, which were measured by Three Gorges Geotechnical Consultants Co., Ltd., almost all measured landslides and debris flows (marked by red and brown polygons, respectively) were located in subsidence areas. In particular, landslides with a large amount of subsidence where the velocity was larger than 30 mm/year (the Jinpingzi landslide and the Dacun-Fujiapingzi landslide group) have become important study objects in ground measurement. The comparison shows that the locating results of SBAS-InSAR were exactly accurate and consistent with the field survey results.

4.2 *Single-Point Monitoring Accuracy*

To test the accuracy of single-point monitoring when using the SBAS-InSAR technique, the LOS displacement values of the leveling points (green dots with black serial numbers on the Jinpingzi landslide in Fig. 16) obtained via SBAS-InSAR were compared with the ground-based ETS survey results. Therefore, the displacement vector d_N, d_E, and d_U in north, east, and up direction, respectively, which were monitored by ETS, will be projected to one slant-range component d_{LOS} in the radar LOS. Equation (12)[50] was used for computing the d_{LOS} value of ETS survey results.

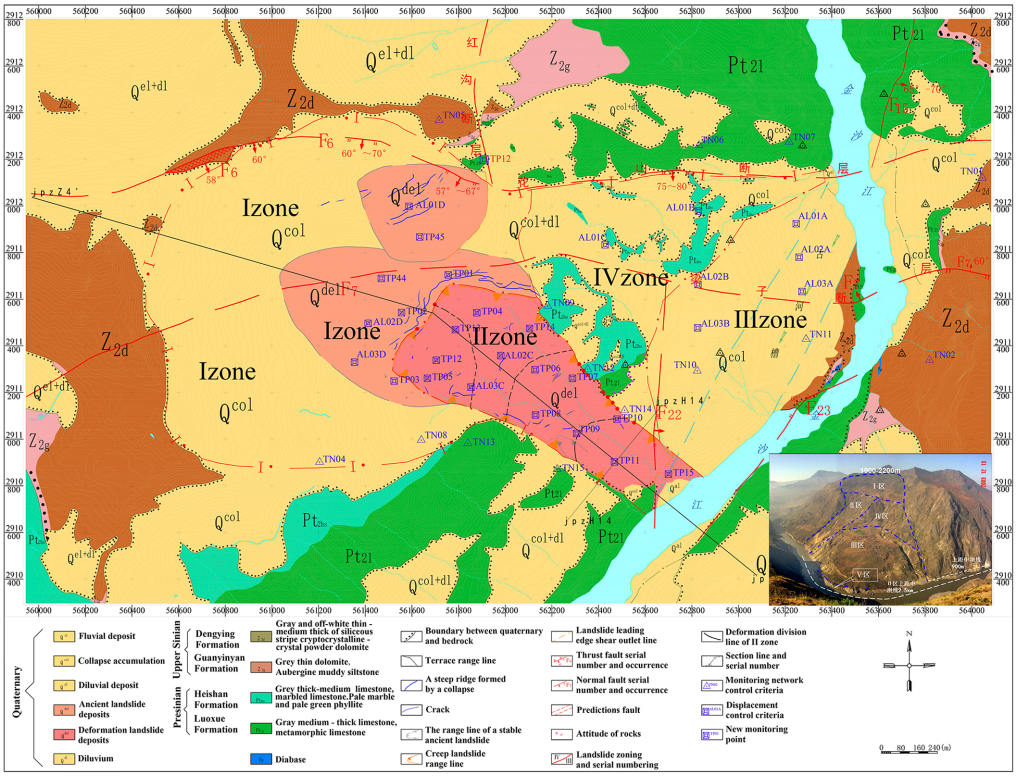

Fig. 13 Geological map of Jinpingzi landslide. An inset picture in the lower right shows the physical environment of the Jinpingzi landslide.

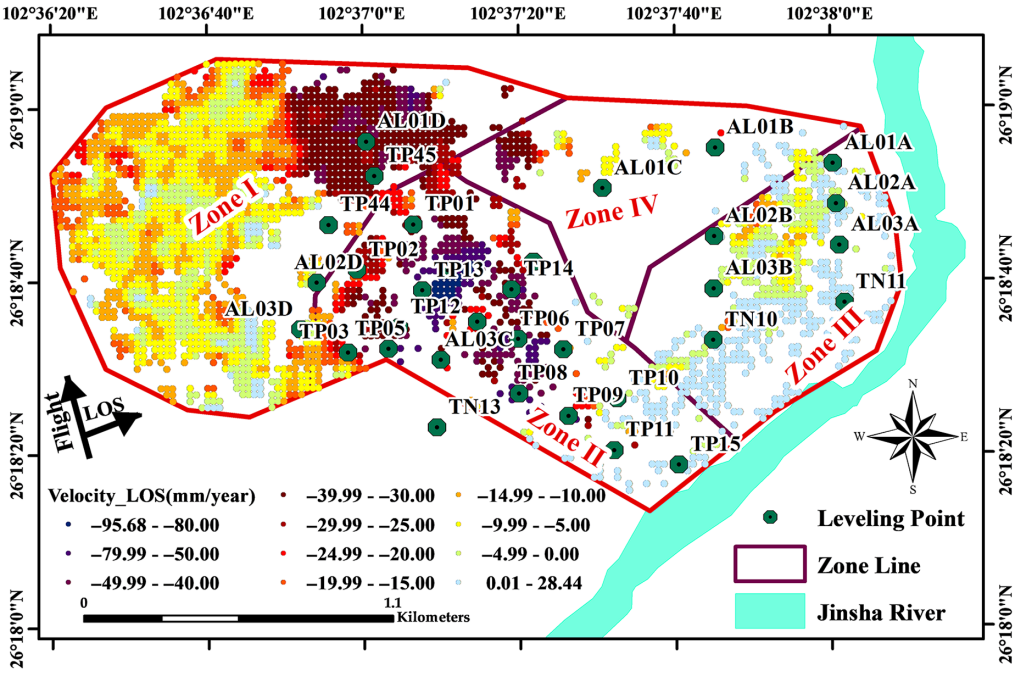

Fig. 14 Velocity map of the Jinpingzi landslide between July 12, 2007, and March 7, 2011, period.

$$d_{\mathrm{LOS}} = d_U \times \cos\theta - \sin\theta \times [d_N \times \cos\omega + d_E \times \sin\omega], \tag{12}$$

where $\theta = 38.737$ deg is the average value of the incidence angle for 19 ascending pass SAR data and $\omega = 174.087$ deg is the average value of the horizontal angles of LOS direction.

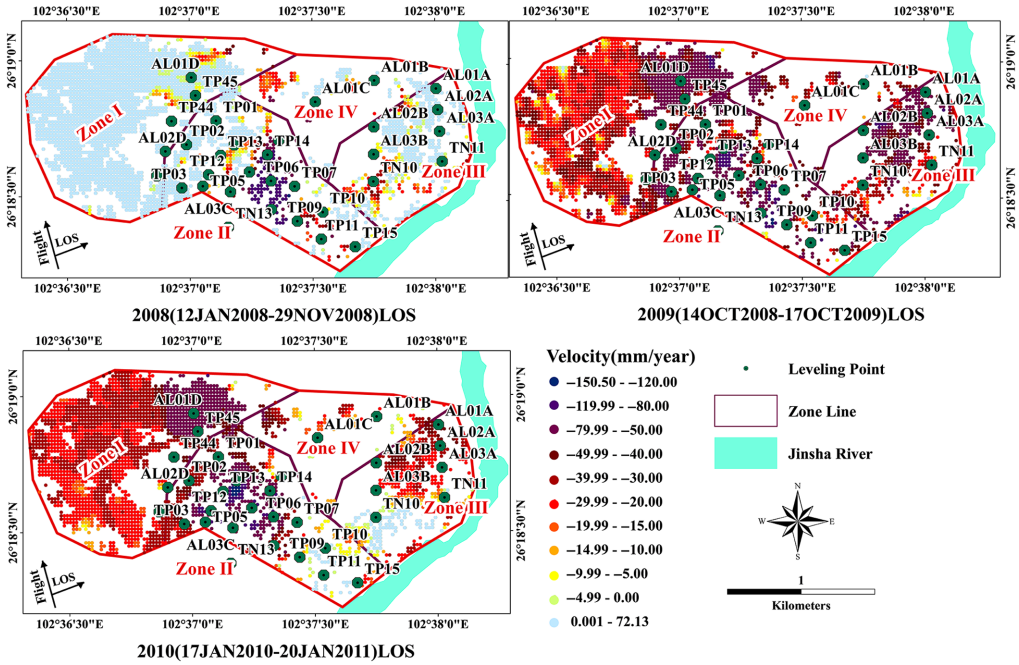

Fig. 15 Annual deformation rate of the Jinpingzi landslide.

Table 2 Comparison of SBAS-InSAR and ETS measurement results (units: mm).

Zone	Point	ETS (LOS/mm) (92 d)	SBAS-InSAR (LOS/mm) (92 d)	ETS (LOS/mm) (368 d)	SBAS-InSAR (LOS/mm) (368 d)
I	AL01D	−14.725	−19.333	−47.903	−36.651
	AL02D	−4.261	−3.078	−6.907	−6.152
	AL03D	−4.117	−4.188	−9.396	−6.930
	TP44	−2.978	−1.493	2.031	2.416
	TP45	−10.678	−9.022	−28.531	−32.875
II	TP01	−4.628	−5.260	−26.886	−34.896
	TP02	−2.745	−3.905	−22.771	−21.075
	TP03	−4.004	−6.266	−19.378	−17.097
	TP04	−41.994	−46.529	−121.299	−105.718
	TP05	−25.023	−32.637	−117.912	−109.515
	TP06	−69.402	−65.100	−130.103	−122.142
	TP07	−53.921	−46.34	−113.643	−105.453
	TP08	−68.761	−62.163	−140.456	−119.848
	TP09	−73.314	−68.058	−145.846	−128.667
	TP10	−56.290	−50.442	−111.276	−114.065
	TP11	−75.499	−69.635	−150.535	−142.149
	TP12	−25.779	−32.864	−109.848	−90.030
	TP13	−25.407	−31.615	−118.684	−109.481

Table 2 (*Continued*).

Zone	Point	ETS (LOS/mm) (92 d)	SBAS-InSAR (LOS/mm) (92 d)	ETS (LOS/mm) (368 d)	SBAS-InSAR (LOS/mm) (368 d)
II	TP14	−63.325	−58.985	−129.2395	−117.472
	TP15	−5.43	−3.519	4.426	3.762
	AL02C	−51.804	−47.289	−69.283	−55.947
	AL03C	−47.454	−35.270	−120.763	−109.730
III	AL01A	0.391	−0.436	−0.393	8.491
	AL02A	1.63	0.806	1.094	2.246
	AL03A	3.714	0.856	−0.484	3.560
	AL02B	−3.461	−6.608	−5.632	−9.124
	AL03B	−1.841	−5.166	−1.895	−3.012
	TN10	−1.626	−4.413	−2.594	−2.853
	TN11	3.208	−1.180	1.233	6.780
IV	AL01B	−3.95	−10.660	−5.057	−21.055
	AL01C	−0.839	−4.763	−6.173	−9.393
Root-mean-square error		Truth value	4.839	Truth value	9.004

When compared with the 92-day (January 12, 2008, to April 13, 2008) SBAS-InSAR results, the ETS survey period was from January 11, 2008, to April 19, 2008, for zone II and from January 12, 2008, to April 18, 2008, for zones I, III, and IV. When compared with the 368-day (July 12, 2007, to July 14, 2008) SBAS-InSAR results, the ETS investigation period was from June 23, 2007, to July 15, 2008, for zone II and from June 28, 2007, to July 14, 2008, for zones I, III, and IV (Table 2). The root-mean-square error was computed, in which the results of the ETS were regarded as the ground-truth values. In addition, a comparison of trend charts in Fig. 17 indicates that the variation trends of SBAS-InSAR results were in perfect agreement with the high-precision ETS data.

5 Conclusions

In this paper, the SBAS-InSAR technique was used to detect and monitor landslides in an alpine valley region located adjacent to Wudongde hydropower reservoir on the Jinsha River. The GLIA, which represents the comprehensive factors of complex topography and satellite attitude parameters, was put forward and put to use, and the noneffective interference areas were calculated and identified using the ascending and descending data by SBAS-InSAR technique. Then, an application example was implemented using the 19 PALSAR-1 acquisitions by the SBAS-InSAR technique, the noneffective interference areas were calculated and excluded, and the monitoring results of the effective interference areas were analyzed in detail. The accuracy of landslide detection was verified by comparison with the ground field survey results in the study area, and the accuracy of single-point monitoring was verified by comparison with high-precision ETS results. The following conclusions can be drawn.

- Due to the effects of regional topography and satellite attitude parameters, TS-InSAR technique cannot effectively identify and monitor all areas in mountainous and valley areas of rugged terrain for landslides. The GLIA can accurately calculate and exclude the areas that cannot be effectively monitored.

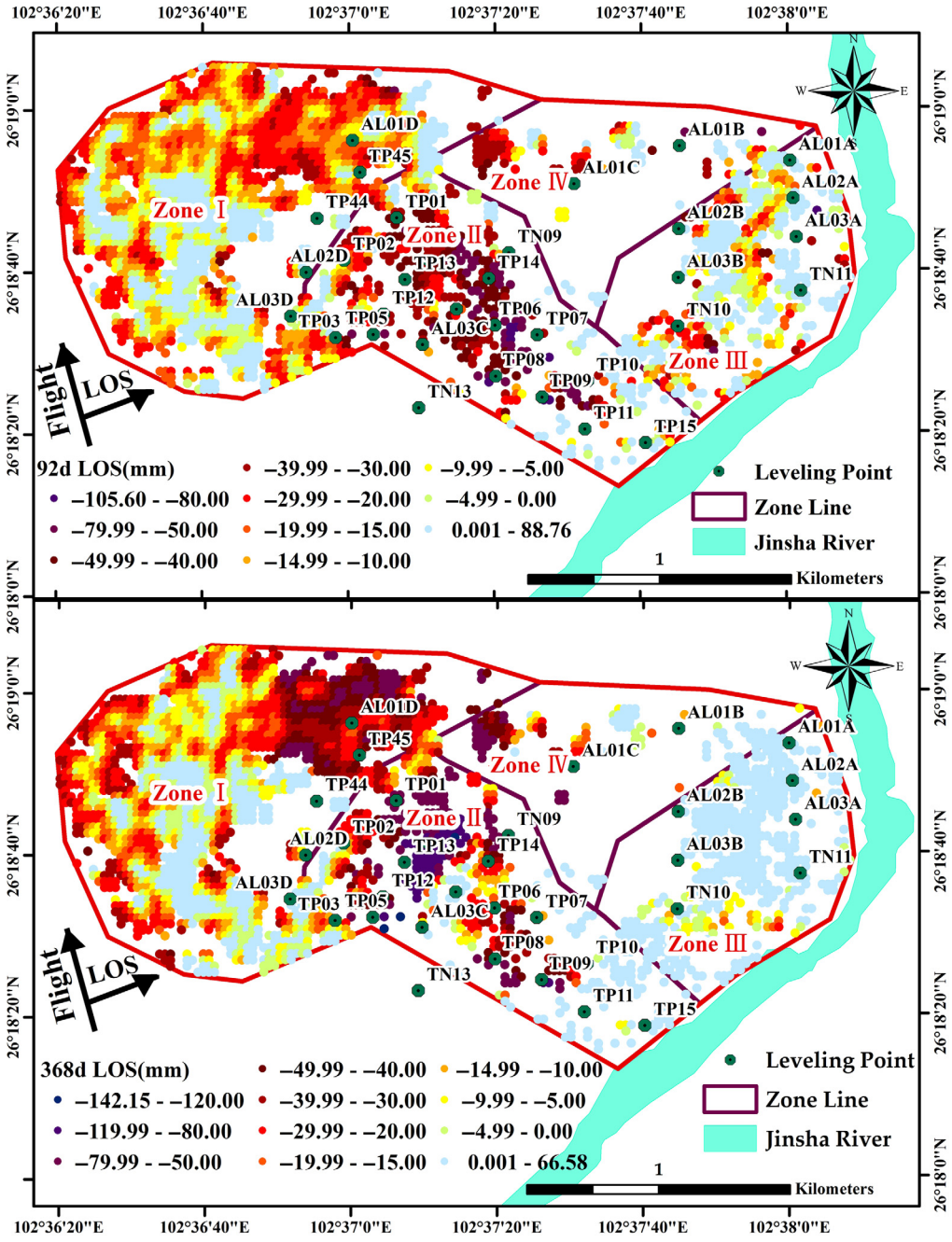

Fig. 16 LOS displacement map of the Jinpingzi landslide (92 days and 368 days).

- The effective range of GLIA is 0 deg to 90 deg for InSAR technology when applied in mountainous and valley areas of rugged terrain. However, the interferometric results of the layover (<0 deg) areas and shadowed (>90 deg) areas were noneffective because of low levels of coherence and geometric distortion.
- In the case of small incident angle difference, the noneffective interference areas are almost consistent for the ascending and descending data. Only the shadowed areas of ascending data are the layover areas of the descending data, and the layover areas of ascending data are the shadowed areas of the descending data.
- Regional landslides locating and single-point monitoring are both very accurate in the effective interferometric areas for landslides monitoring using the SBAS-InSAR technique. This study provides a new idea and reference for the early identification and high-precision monitoring of landslides in mountainous and valley areas applying TS-InSAR technology.

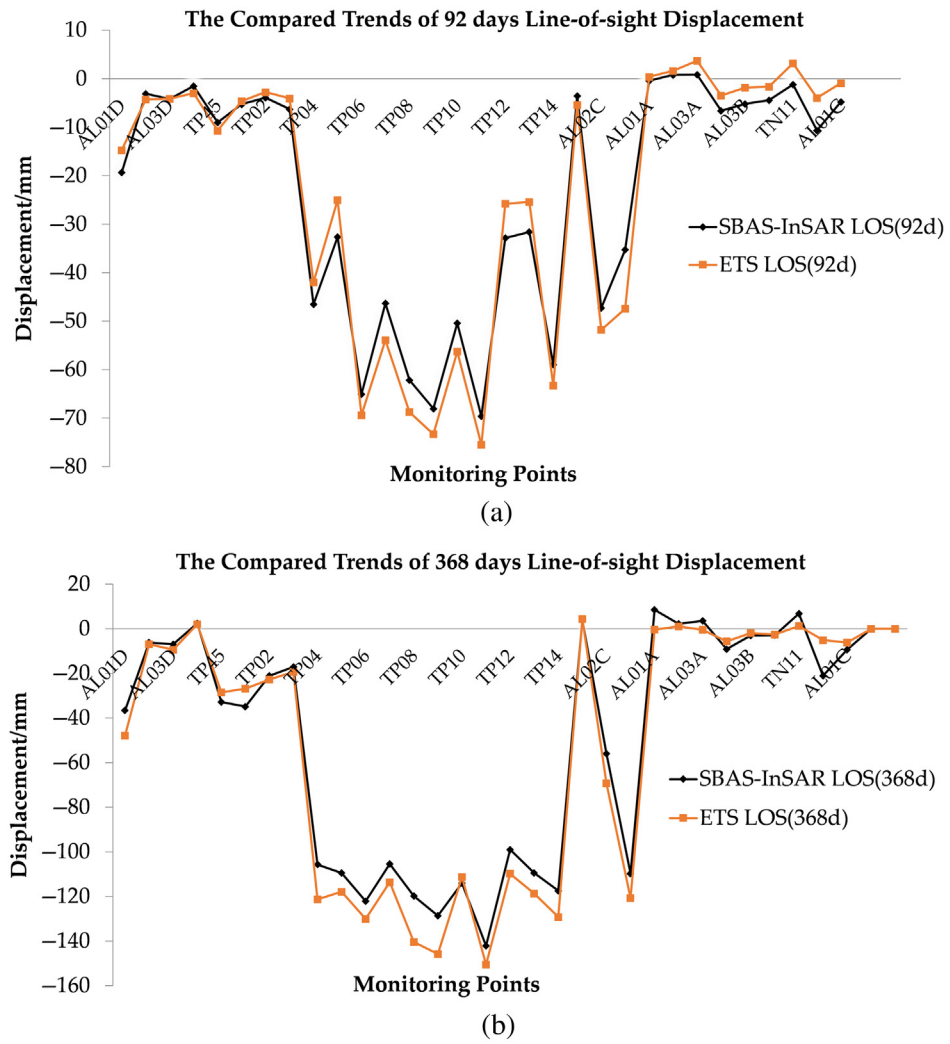

Fig. 17 LOS displacement trends for SBAS-InSAR and ETS (unit: mm). The compared trends of (a) 92 days LOS displacement and (b) 386 days LOS displacement.

Acknowledgments

The authors thank the Japan Aerospace Exploration Agency, which provided the PALSAR data (PI No. 3031). The authors thank Three Gorges Geotechnical Consultants Co., Ltd. and the University of Science and Technology Beijing, which provided the detailed on-ground monitoring data. This research was funded by the National Natural Science Foundation of China (Grant No. 41572309), the China Geological Survey (Grant No. DD20190679), and National Key Research and Development Program of China (Ministry of Science and Technology of the People's Republic of China) (Grant No. 2017YFC1502502). The authors declare no conflicts of interest.

References

1. J. Achache, B. Fruneau, and C. Delacourt, "Applicability of SAR interferometry for operational monitoring of landslides," in *Proc. Second ERS Appl. Workshop*, London, pp. 165–168 (1995).
2. B. Fruneau, J. Achace, and C. Delacourt, "Observation and modeling of the Sant-Etienne-de Tine'e landslide using SAR interferometry," *Tectonophysics* **265**, 181–190 (1996).
3. J. Vietmeier, W. Wagner, and R. Dikau, "Monitoring moderate slope movements (landslides) in the southern French Alps using differential SAR interferometry," in *Proc. FRINGE*, Liège, Belgium (1999).

4. V. Rizzo and M. Tesauro, "SAR interferometry and field data of Randazzo landslide (eastern Sicily, Italy)," *Phys. Chem. Earth Part B* **25**, 771–780 (2000).
5. C. Squarzoni, C. Delacourt, and P. Allemand, "Nine years of spatial and temporal evolution of the La Valette landslide observed by SAR interferometry," *Eng. Geol.* **68**, 53–66 (2003).
6. P. Berardino et al., "Use of differential SAR interferometry in monitoring and modelling large slope instability at Maratea (Basilicata, Italy)," *Eng. Geol.* **68**, 31–51 (2003).
7. F. Catani et al., "On the application of SAR interferometry to geomorphological studies: estimation of landform attributes and mass movements," *Geomorphology* **66**, 119–131 (2005).
8. B. Riedel and A. Walther, "InSAR processing for the recognition of landslides," *Adv. Geosci.* **14**, 189–194 (2008).
9. M. S. Liao et al., "Landslide monitoring with high-resolution SAR data in the Three Gorges region," *Sci. China Earth Sci.* **59**, 590–601 (2011).
10. G. J. Wang et al., "Application of D-INSAR technique to landslide monitoring," *Rock Soil Mech.* **31**, 1337–1343 (2010), in Chinese.
11. G. J. Wang et al., "Experiment research of D-InSAR technique on identifying landslide moving in a wide area," *J. Univ. Sci. Technol. Beijing* **33**, 131–141 (2013), in Chinese.
12. G. J. Wang et al., "D-InSAR-based landslide location and monitoring at Wudongde hydropower reservoir in China," *Environ. Earth Sci.* **69**, 2763–2777 (2013).
13. A. Ferretti, C. Prati, and F. Rocca, "Permanent scatterers InSAR interferometry," *IEEE Trans. Geosci. Remote Sens.* **39**, 8–20 (1999).
14. P. Berardino et al., "A new algorithm for surface deformation monitoring based on small baseline differential SAR interferograms," *IEEE Trans. Geosci. Remote Sens.* **40**, 2375–2383 (2002).
15. O. Mora, J. J. Mallorqui, and A. Broquetas, "Linear and nonlinear terrain deformation maps from a reduced set of interferometric SAR images," *IEEE Trans. Geosci. Remote Sens.* **41**, 2243–2253 (2003).
16. A. Arnaud et al., "ASAR ERS interferometric phase continuity," in *Proc. IEEE Int. Geosci. and Remote Sens. Symp.*, Toulouse, France, pp. 1133–1135 (2003).
17. A. Hooper, H. Zebker, and P. Segall, "A new method for measuring deformation on volcanoes and other natural terrains using InSAR persistent scatters," *Geophys. Res. Lett.* **31**, L23611 (2004).
18. A. Ferretti et al., "A new algorithm for processing interferometric data-stacks: SqueeSAR," *IEEE Trans. Geosci. Remote Sens.* **49**, 3460–3470 (2011).
19. F. Colesanti et al., "Monitoring landslides and tectonic motions with the permanent scatterers technique," *Eng. Geol.* **68**, 3–14 (2003).
20. Z. Perski et al., "InSAR analyses of terrain deformation near the Wieliczka Salt Mine," *Eng. Geol.* **106**, 58–67 (2009).
21. G. Nico et al., "On the statistical properties of persistent scatterers location to discriminate landslide predisposing factors," in *Proc. FRINGE*, Frascati, Italy (2009).
22. V. Greif and J. Vlcko, "Monitoring of post-failure landslide deformation by the PS-InSAR technique at Lubietova in central Slovakia," *Earth Sci.* **66**, 1585–1595 (2012).
23. P. Tantianuparp et al., "Characterization of landslide deformations in Three Gorges area using multiple InSAR data stacks," *Remote Sens.* **5**, 2704–2719 (2013).
24. F. Raspini, S. Moretti, and N. Casagli, "Landslide mapping using SqueeSAR data: Giampilieri (Italy) case study," *Landslide Sci. Pract.* **1**, 147–154 (2013).
25. L. Lanteri and A. Colombo, "The integration between satellite data and conventional monitoring system in order to update the Arpa Piemonte landslide inventory," *Landslide Sci. Pract.* **1**, 135–140 (2013).
26. C. Meisina et al., "The use of PSInSAR™ and SqueeSAR™ techniques for updating landslide inventories," *Landslide Sci. Pract.* **1**, 81–87 (2013).
27. P. Liu et al., "Using advanced InSAR time series techniques to monitor landslide movements in Badong of the Three Gorges region," *Int. J. Appl. Earth Obs. Geoinf.* **21**, 253–264 (2013).
28. A. Novellino et al., "Intermittent small baseline subset (ISBAS) InSAR analysis to monitor landslides in Costa Della Gaveta, Southern Italy," in *Proc. Int. Geosci. Remote Sens. Symp.*, Milan, Italy, pp. 3536–3539 (2015).

29. P. Confuorto et al., "Post-failure evolution analysis of a rainfall-triggered landslide by multitemporal interferometry SAR approaches integrated with geotechnical analysis," *Remote Sens. Environ.* **188**, 51–72 (2017).
30. M. Costantini et al., "Analysis of surface deformations over the whole Italian territory by interferometric processing of ERS, Envisat and COSMO-SkyMed radar data," *Remote Sens. Environ.* **202**, 250–275 (2017).
31. D. D. Martirea et al., "A nation-wide system for landslide mapping and risk management in Italy: the second not-ordinary plan of environmental remote sensing," *Int. J. Appl. Earth Obs. Geoinf.* **63**, 143–157 (2017).
32. S. Bianchini et al., "Detecting and monitoring landslide phenomena with TerraSAR-X persistent scatterers data: the Gimigliano case study in Calabria Region (Italy)," in *Proc. IEEE Geosci. and Remote Sens. Symp.*, Munich, Germany, pp. 982–985 (2012).
33. F. Cigna, S. Bianchini, and N. Casagli, "How to assess landslide activity and intensity with persistent scatterer interferometry (PSI) the PSI-based matrix approach," *Landslides* **10**, 267–283 (2013).
34. F. Raspini et al., "Exploitation of amplitude and phase of satellite SAR images for landslide mapping: the case of Montescaglioso (South Italy)," *Remote Sens.* **7**, 14576–14596 (2015).
35. M. H. Li et al., "Monitoring active motion of the Guobu landslide near the Laxiwa Hydropower Station in China by time-series point-like targets offset tracking," *Remote Sens. Environ.* **221**, 80–93 (2019).
36. M. Peyret et al., "Monitoring of the large slow Kahrod landslide in Alborz mountain range (Iran) by GPS and SAR interferometry," *Eng. Geol.* **100**, 131–141 (2008).
37. Y. P. Yin et al., "Integration of GPS with InSAR to monitoring of the Jiaju landslide in Sichuan," *Landslides* **7**, 359–365 (2010).
38. M. Akbarimehr, M. Motagh, and M. Haghshenas-Haghighi, "Slope stability assessment of the Sarcheshmeh landslide, northeast Iran, investigated using InSAR and GPS observations," *Remote Sens.* **5**, 3681–3700 (2013).
39. W. Zhu et al., "Landslide monitoring by combining of CR-InSAR and GPS techniques," *Adv. Space Res.* **53**, 430–439 (2014).
40. D. D. Martire et al., "Quaternary deformation in SE Sicily: insights into the life and cycles of forebulge fault systems," *Lithosphere* **7**, 519–534 (2015).
41. F. Cigna et al., "25 years of satellite InSAR monitoring of ground instability and coastal geohazards in the archaeological site of Capo Colonna, Italy," *Proc. SPIE* **10003**, 100030Q (2016).
42. T. Carlà et al., "Integration of ground-based radar and satellite InSAR data for the analysis of an unexpected slope failure in an open-pit mine," *Eng. Geol.* **235**, 39–52 (2018).
43. G. Farolfi, S. Bianchini, and N. Casagli, "Integration of GNSS and satellite InSAR data: derivation of fine-scale vertical surface motion maps of Po Plain, Northern Apennines, and Southern Alps, Italy," *IEEE Trans. Geosci. Remote Sens.* **57**, 319–328 (2019).
44. B. A. Pour and M. Hashim, "Application of Landsat-8 and ALOS-2 data for structural and landslide hazard mapping in Kelantan, Malaysia," *Nat. Hazards Earth Syst. Sci.* **17**, 1285–1303 (2017).
45. M. Hashim, S. Misbari, and B. A. Pour, "Landslide mapping and assessment by integrating Landsat-8, PALSAR-2 and GIS techniques: a case study from Kelantan state, peninsular Malaysia," *J. Indian Soc. Remote Sens.* **46**, 233–248 (2018).
46. S. Plank et al., "Pre-survey suitability evaluation of the differential synthetic aperture radar interferometry method for landslide monitoring," *Int. J. Remote Sens.* **33**, 6623–6637 (2012).
47. D. Notti et al., "A methodology for improving landslide PSI data analysis," *Int. J. Remote Sens.* **35**, 2186–2214 (2014).
48. G. J. Wang et al., "InSAR-based landslide location and monitoring in Alpine Valley region," in *Landslide Science for a Safer Geoenvironment*, K. Sassa, P. Canuti, and Y. Yin, Eds., pp. 379–388, Springer, Switzerland (2014).
49. M. W. Xie et al., "The characteristic analysis of D-InSAR data for landslides monitoring in Alpine and Canyon region," *Bull. Surv. Mapp.* **4**, 18–21 (2012), in Chinese.

50. R. F. Hanssen, "Radar system theory and interferometric processing," in *Radar Interferometry: Data Interpretation and Error Analysis*, F. van der Meer, Ed., Vol. **2**, pp. 9–60, Kluwer Academic Publishers, New York (2001).

Guijie Wang is a professor at China Institute of Geo-Environment Monitoring. She received her doctoral degree in geotechnical engineering from the University of Science and Technology Beijing in 2010. She has long been engaged in the application research of SAR remote sensing technology in the field of geological disaster investigation and monitoring, and has presided over the completion of many national and provincial projects. She is the author of more than 20 journal papers.

Yunlong Wang is an engineer at the China Institute of Geo-Environment Monitoring. He received his master's degrees in geological environment and engineering from China University of Geosciences Beijing in 2010. He has long been engaged in the research of geological disasters in the field of land subsidence and ground fissures.

Xisheng Zang is an engineer at China Institute of Geo-Environment Monitoring. He received his master's degree in China University of Geoscience Beijing in 2013. He has long been engaged in the hydrological and environmental geologic survey and research, and has participated in completion of many national and provincial projects.

Juyan Zhu is a senior engineer at China Institute of Geo-Environment Monitoring. She received her doctorate in groundwater science and engineering from the China University of Geoscience Beijing in 2014. Her research is focus on groundwater and land subsidence, and she is the author of more than eight papers.

Weilun Wu: Biography is not available.